



HAL
open science

Spectral analysis of the small-scale directional anisotropy in forced homogeneous rotating turbulence

Donato Vallefucoco, Fabien Godeferd, Aurore Naso

► **To cite this version:**

Donato Vallefucoco, Fabien Godeferd, Aurore Naso. Spectral analysis of the small-scale directional anisotropy in forced homogeneous rotating turbulence. CFM 2017 - 23ème Congrès Français de Mécanique, Aug 2017, Lille, France. hal-03465595

HAL Id: hal-03465595

<https://hal.science/hal-03465595>

Submitted on 3 Dec 2021

HAL is a multi-disciplinary open access archive for the deposit and dissemination of scientific research documents, whether they are published or not. The documents may come from teaching and research institutions in France or abroad, or from public or private research centers.

L'archive ouverte pluridisciplinaire **HAL**, est destinée au dépôt et à la diffusion de documents scientifiques de niveau recherche, publiés ou non, émanant des établissements d'enseignement et de recherche français ou étrangers, des laboratoires publics ou privés.

Spectral analysis of the small-scale directional anisotropy in forced homogeneous rotating turbulence

D. VALLEFUOCO^a, F.S. GODEFERD^a, A. NASO^a

a. Laboratoire de Mécanique des Fluides et d'Acoustique,
CNRS (UMR 5509), Université de Lyon,
École Centrale de Lyon, Université Claude Bernard Lyon 1, INSA Lyon, France

Résumé :

Dans ce travail sont effectuées des simulations numériques directes pseudo-spectrales, à haute résolution, d'écoulements turbulents en rotation, hélicitaires ou non, à grand nombre de Reynolds et dans un domaine périodique 3D. La dépendance en échelle de l'anisotropie est étudiée grâce à la mesure de spectres d'énergie et d'hélicité dépendant de la direction dans l'espace de Fourier. On s'intéresse au régime de faible rotation, dans lequel la grande séparation d'échelles permet d'étudier les effets d'anisotropie à des échelles beaucoup plus petites que l'échelle de Zeman. On met en évidence l'existence d'une gamme de faibles nombres d'ondes auxquelles l'écoulement est très anisotrope, et d'une gamme de grands nombres d'onde auxquels l'anisotropie de l'écoulement est plus faible. L'un des résultats marquants de cette étude est le fait que le niveau d'anisotropie reste significatif aux plus petites échelles résolues (bien qu'il décroisse à nombre de Rossby croissant), contrairement à des résultats numériques récents, mais en accord avec des résultats expérimentaux. Finalement, on estime la valeur du nombre d'onde séparant les grands (faiblement anisotropes) des petits (fortement anisotropes) nombres d'onde, et fournissons une interprétation physique de celui-ci.

Abstract :

In this work, we perform high resolution pseudo-spectral direct numerical simulations of non-helical and helical forced rotating turbulence at high Reynolds number in a 3D periodic domain. The scale-dependence of anisotropy is characterized through energy and helicity direction-dependent spectra in the Fourier space. We focus on the low rotation regime, in which the large scale separation permits to study the anisotropic features of scales much smaller than the Zeman scale. We evidence the existence of a highly anisotropic small-wavenumber range and of a weakly anisotropic large-wavenumber range. Importantly, it is observed that the anisotropy level is still significant at the smallest resolved scales (although it decreases as the Rossby number increases), in contrast with recent numerical results, but in agreement with some experiments. Finally, we estimate the value of the threshold wavenumber between large-anisotropy wavenumbers and low-anisotropy wavenumbers, and provide a physical interpretation for it.

Mots clefs : Turbulence, Rotation, Anisotropy, Direct numerical simulation

1 Introduction

Rotating turbulence is relevant in many contexts, for instance geophysical and industrial flows, or academic configurations such as the von Kármán-forced turbulence [1]. It is nowadays commonly admitted that background rotation introduces a significant anisotropy in the turbulent dynamics through both linear and nonlinear mechanisms (see *e.g.* [2]). In this work, we characterize the effect of rotation on the scale-dependent anisotropy of turbulence by investigating the energy and helicity directional anisotropies in Fourier space, *i.e.* spectra of energy and helicity that depend on the orientation.

In homogeneous and rotating turbulence, the flow regime can be characterized by two independent non-dimensional parameters. One possible choice is the Reynolds number $Re^L = UL/\nu$ and the macro-Rossby number $Ro^L = U/(2\Omega L)$, where U is a large-scale characteristic velocity [*e.g.* the root-mean square (r.m.s.) velocity], L is a large-scale characteristic lengthscale (*e.g.* the integral scale), ν is the kinematic viscosity, and Ω is the rotation rate. The micro-Rossby number is defined as $Ro^\omega = \omega'/(2\Omega)$, where ω' is the r.m.s. vorticity. The macro- and the micro-Rossby numbers quantify the relative importance of advection with respect to rotation. In addition to L , three more characteristic lengthscales can be defined : the Kolmogorov scale $\eta = (\nu^3/\epsilon)^{1/4}$, where ϵ is the mean energy dissipation rate ; the scale at which the inertial timescale $(r^2/\epsilon)^{1/3}$ equals the rotation timescale $1/\Omega$, $r_\Omega = \sqrt{\epsilon/(2\Omega)^3}$ [3, 4], referred to as the Zeman scale ; the scale at which the dissipative timescale r^2/ν equals the rotation timescale, $r_{\Omega d} = \sqrt{\nu/(2\Omega)}$. From the above definitions of η and r_Ω , $r_{\Omega d} = r_\Omega^{1/3}\eta^{2/3}$. One alternative choice for the independent parameters may be two characteristic lengthscale ratios. Furthermore, by setting $\epsilon \sim U^3/L$, the ratio of the integral scale to the Kolmogorov scale and the ratio of the Zeman scale to the integral scale are linked to Re^L and Ro^L : $L/\eta \sim Re^{L^{3/4}}$ and $r_\Omega/L \sim Ro^{L^{3/2}}$. Similarly, if $\omega' \sim \nu/\eta^2$, $Ro^\omega \sim (r_\Omega/\eta)^{2/3}$ and $\epsilon \sim U^3/L$ also leads to $Ro^\omega \sim (Re^L)^{1/2}Ro^L$. The assumption that $\epsilon \sim U^3/L$ at high Reynolds numbers has been extensively investigated in isotropic turbulence and a precise scaling law for $C_\epsilon = \epsilon/(U^3L)$ has been obtained for non-equilibrium (*e.g.* decaying) turbulence (see [5] for a review), but for forced turbulence C_ϵ has been found to be constant and independent of the forcing scheme and the forcing wavenumber, even if turbulence is quasi-periodic and time averages are considered, see [6, 7]. Note that Ro^ω (or the equivalent parameters r_Ω/η and $Re^L Ro^{L^2}$) does not depend on large-scale characteristic quantities like the integral lengthscale or the r.m.s. velocity, and is indeed the only nondimensional parameter that arises from a dimensional analysis if only ϵ , ν and Ω are taken into account. In the following sections we will refer to characteristic wavenumbers instead of lengthscales : $k_\eta = 1/\eta$, $k_\Omega = 1/r_\Omega$ and $k_{\Omega d} = 1/r_{\Omega d}$.

If the Reynolds number tends to infinity, both η and $r_{\Omega d}$ tend to zero. The only relevant small-scale characteristic lengthscale is then r_Ω , which is the scale where the characteristic rotation time equals the characteristic inertia time. For this reason, according to classical dimensional arguments, in the asymptotically inviscid limit, scales much larger than r_Ω are strongly affected by rotation and should be more anisotropic, while scales much smaller than r_Ω are dominated by the nonlinear dynamics and are expected to recover isotropy. However, only finite Reynolds number turbulence can be tackled through simulations and experiments, and very large Reynolds numbers are needed to achieve a good scale separation. Direct numerical simulations (DNS) by [8, 9] seem to confirm isotropy recovery at small scales, while in experiments by [10] the anisotropy is found to be stronger at small scales. In particular, in the forced rotating simulation of [9], which has $Ro^\omega = 2.25$, isotropization seems to occur at a precise

wavenumber (close to k_Ω). In [8], in which decaying rotating turbulence is investigated, isotropy is recovered only if rotation is weak enough, and a link between k_Ω and the wavenumber corresponding to maximum anisotropy is observed. Therefore, since both the anisotropic character of small scales and the role of the Zeman scale are not fully understood, we investigate here small-scale anisotropy in rotating turbulence through high resolution forced DNS with large scale separation, up to $r_\Omega/\eta = 68$.

The paper is organized as follows. In sections 2 and 3 we respectively introduce the refined two-point statistics used in the following as diagnostics for anisotropy characterization, and present the numerical simulation method and the Euler forcing scheme. Section 4 is devoted to the evaluation of anisotropy induced by background rotation in homogeneous non-helical and helical turbulence. In section 5 two different anisotropic ranges are identified, and a scaling law for the separating scale is provided. Conclusions are drawn in section 6.

2 Fine-grained anisotropy in two-point statistics

The characterization of anisotropy in homogeneous turbulence addresses a two-fold question. First, what physical quantities are suitable to qualitatively detect isotropy breaking in turbulence subject to external distortions such as solid body rotation, density gradient, mean shear, *etc.*? Second, how does one quantify and compare the level of anisotropy? One therefore needs a relevant characterization of this anisotropy, and several choices are possible. In the present section we describe in detail the statistical indicators we use to evaluate scale- and direction-dependent anisotropy of the velocity field.

Considering the Reynolds stress tensor \mathbf{R} of components $R_{ij}(\mathbf{r}, t) = \langle u_i(\mathbf{x}, t)u_j(\mathbf{x} + \mathbf{r}, t) \rangle$, where $\mathbf{x} = (x, y, z)$ is the Cartesian coordinate in physical space, \mathbf{r} is the separation vector, t is time and $\langle \rangle$ represents ensemble averaging, one can obtain the components of the anisotropic part of \mathbf{R} , $b_{ij} = R_{ij}/R_{kk} - \delta_{ij}/3$. If the off-diagonal components of \mathbf{b} are not zero the flow is anisotropic, but these quantities only represent anisotropy from a global point of view—mostly related to the large scales. A widely adopted characterization of anisotropy based on \mathbf{b} is the method proposed by Lumley & Newman (1977) [11] which consists in identifying the dominant structure of the flow from the position of the second and third invariants (I_2, I_3) of \mathbf{b} within the so-called Lumley triangle. This tells if the flow structure is mostly 2-component axisymmetric, 1-component, or isotropic, depending on the closeness of the (I_2, I_3) point to one of the vertices of the triangle. However, useful as this simple method may be, it does not tell which scales are most anisotropic. A refined picture is for instance required for rotating turbulence, in which one has to identify isotropic and anisotropic subranges at different length scales (see section 4).

We therefore introduce hereafter a scale-by-scale evaluation of anisotropy, assuming statistical axisymmetry of the flow. In addition to the length scale or wavenumber, we also retain the dependence of the spectra on the polar angle about the axis of symmetry. This description is suitable for a wide range of anisotropic flows, such as turbulence subject to solid body rotation, stratified turbulence, flows subject to axisymmetric contractions or expansions or more generally axisymmetric strain, magneto-hydrodynamic turbulence for a conducting fluid subject to an external magnetic field of fixed orientation. Non axisymmetric cases are more complex and only a few studies have been devoted to their statistical description.

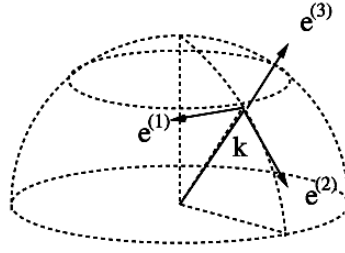


FIGURE 1 – Craya-Herring frame of reference.

2.1 Modal decomposition of the Reynolds-stress tensor spectrum

Since we deal with homogeneous turbulent flows, the two-point correlation tensor \mathbf{R} is independent of \mathbf{x} , and—if it tends to zero sufficiently rapidly as $|\mathbf{r}|$ increases—we can consider its Fourier transform

$$\hat{R}_{ij}(\mathbf{k}) = \frac{1}{(2\pi)^3} \iiint R_{ij}(\mathbf{r}) e^{-i\mathbf{k}\cdot\mathbf{r}} d^3\mathbf{r} \quad (1)$$

(for simplicity, we drop here the dependence upon time t). Note that the incompressibility condition $\nabla \cdot \mathbf{u} = 0$ implies $\partial R_{ij}(\mathbf{r})/\partial r_j = 0$, which by Eq. (1) leads to $\hat{R}_{ij}(\mathbf{k})k_j = 0$. Furthermore, since $R_{ij}(\mathbf{r})$ is real and $R_{ij}(\mathbf{r}) = R_{ji}(-\mathbf{r})$ from its definition, $\hat{R}_{ij}(\mathbf{k})$ is a Hermitian matrix, *i.e.* $\hat{R}_{ij}^*(\mathbf{k}) = \hat{R}_{ji}(\mathbf{k})$, where * stands for complex conjugate. It is useful to project the tensor $\hat{\mathbf{R}}$ onto a polar-spherical orthonormal basis $(\mathbf{e}^{(1)}, \mathbf{e}^{(2)}, \mathbf{e}^{(3)})$ defined from the vector \mathbf{n} bearing the axis of symmetry, with

$$\mathbf{e}^{(1)} = \frac{\mathbf{k} \times \mathbf{n}}{|\mathbf{k} \times \mathbf{n}|}, \quad \mathbf{e}^{(2)} = \mathbf{e}^{(3)} \times \mathbf{e}^{(1)}, \quad \mathbf{e}^{(3)} = \frac{\mathbf{k}}{k}, \quad (2)$$

which is the so-called Craya-Herring frame [12], see Fig. 1. $\mathbf{e}^{(1)}$ and $\mathbf{e}^{(2)}$ are respectively referred to as *toroidal* and *poloidal* directions. By enforcing incompressibility and Hermitian symmetry

$$\hat{R}_{ij}(\mathbf{k}) = \Phi^1(\mathbf{k})\mathbf{e}^{(1)}\mathbf{e}^{(1)} + \Phi^{12}(\mathbf{k})\mathbf{e}^{(1)}\mathbf{e}^{(2)} + \Phi^{12*}(\mathbf{k})\mathbf{e}^{(2)}\mathbf{e}^{(1)} + \Phi^2(\mathbf{k})\mathbf{e}^{(2)}\mathbf{e}^{(2)} \quad (3)$$

where $\Phi^1/2$ and $\Phi^2/2$ are the toroidal and the poloidal energy spectral densities. Equation (3) can be rewritten as [13, 14]

$$\hat{R}_{ij}(\mathbf{k}) = e(\mathbf{k})P_{ij}(\mathbf{k}) + \Re(z(\mathbf{k})N_i(\mathbf{k})N_j(\mathbf{k})) + ih(\mathbf{k})\epsilon_{ijl}\frac{k_l}{2k^2} \quad (4)$$

where $P_{ij} = \delta_{ij} - k_i k_j/k^2$ is the projector onto the $(\mathbf{e}^{(1)}, \mathbf{e}^{(2)})$ plane, $\mathbf{N}(\mathbf{k}) = \mathbf{e}^{(2)}(\mathbf{k}) - i\mathbf{e}^{(1)}(\mathbf{k})$ are helical modes [15], ϵ_{ijk} is the alternating Levi-Civita tensor, and \Re denotes the real part. The decomposition (4) displays three important spectral functions which characterize fully the second-order velocity correlations of the flow and carry useful physical meaning about the flow structure at different scales [14, 13, 8]:

1. $e(\mathbf{k}) = \hat{R}_{ii}(\mathbf{k})/2 = (\Phi^1(\mathbf{k}) + \Phi^2(\mathbf{k}))/2$ is the spectral energy density, and upon integration over spherical shells of radius $k = |\mathbf{k}|$ provides the kinetic energy spectrum $E(k) = \int e(\mathbf{k})\delta(|\mathbf{k}| - k) d\mathbf{k}$ that scales as $k^{-5/3}$ in the inertial range of high Reynolds number isotropic turbulence according to Kolmogorov theory. If energy is concentrated in modes corresponding to wavevectors close to the plane $\mathbf{k} \cdot \mathbf{n} = 0$ the flow is almost bidimensional, while energy

concentrated in wavevectors close to \mathbf{n} indicates a trend towards a vertically-sheared horizontal flow.

2. The complex-valued function

$$z(\mathbf{k}) = (\Phi^2(\mathbf{k}) - \Phi^1(\mathbf{k})) / 2 + i\Im\Phi^{12}(\mathbf{k}) \quad (5)$$

is the polarization spectral density and contains information on the structure of the flow at different scales. Detailed comments about the role of z in rotating turbulence or MHD turbulence can be found in [14, 16, 8].

3. Finally, $h(\mathbf{k}) = 2k\Im\Phi^{12}(\mathbf{k})$ (where \Im stands for imaginary part) is the helicity spectral density. In physical space, helicity density is the scalar product between velocity and vorticity, $\mathcal{H} = \mathbf{u} \cdot \boldsymbol{\omega}$, and—exactly like energy—its integral is an inviscid invariant [17, 18] (even in the presence of background rotation). $h(\mathbf{k})$ is the Fourier transform of the velocity-vorticity correlation $\langle \mathbf{u}(\mathbf{x}) \cdot \boldsymbol{\omega}(\mathbf{x} + \mathbf{r}) \rangle$, and thus $\int h(\mathbf{k}) d\mathbf{k}$ equals the mean helicity $\langle \mathcal{H} \rangle$. The helicity spectrum is

$$H(k) = \int h(\mathbf{k}) \delta(|\mathbf{k}| - k) d\mathbf{k}. \quad (6)$$

Since helicity is a pseudoscalar quantity, any turbulent flow with non-vanishing mean helicity lacks mirror-symmetry. However, in section 4 we will focus on directional anisotropy, and the word “anisotropic” will refer to any isotropy breaking but mirror-symmetry breaking.

2.2 Directional dependence of the spectra

In the above decomposition, axisymmetry is used for decomposing the tensor $\hat{\mathbf{R}}$, but we have retained the general \mathbf{k} dependence. One can further use axisymmetry to consider only the dependence of the spectra upon the axial and horizontal components of the wavevector \mathbf{k} (see for instance [19]), or upon the wavenumber k and the polar orientation θ of \mathbf{k} with respect to the axis of symmetry [20, 21]. Therefore, in our following analysis of spectral anisotropy, we shall present θ -dependent spectra of energy and helicity, discretizing k between minimal and maximal values set by the computational box size and the resolution, and considering angular averages of spectra in five equal angular sectors in the interval $\theta \in [0, \pi/2]$, *i.e.* $[(i-1)\pi/10, i\pi/10]$ with $i = 1, \dots, 5$. The resulting angular spectra, obtained by partial integration of the corresponding spectral densities over these sectors, will be denoted as $E_i(k)$ (energy) and $H_i(k)$ (helicity). Note that the spectra for all angular sectors are normalised such that for directionally isotropic turbulence they collapse onto the corresponding spherically-integrated spectrum, *e.g.* $E_i(k)$ spectra collapse on $E(k)$. The limited number of sectors is imposed by the need of a minimal number of discrete wavevectors in every sector for achieving decent sample size from DNS data. Even so, in the small wavenumbers, very few wavevectors naturally lie within the averaging regions.

3 Numerical set-up

We consider an incompressible fluid whose motion follows the Navier-Stokes equations

$$\begin{aligned} \frac{\partial \mathbf{u}}{\partial t} + (\boldsymbol{\omega} + 2\boldsymbol{\Omega}) \times \mathbf{u} &= -\nabla P + \nu \nabla^2 \mathbf{u} + \mathbf{F} \\ \nabla \cdot \mathbf{u} &= 0 \end{aligned} \quad (7)$$

where \mathbf{u} is the fluctuating velocity field, $\boldsymbol{\omega} = \nabla \times \mathbf{u}$ is the vorticity, P is the total pressure (sum of the hydrodynamic pressure and the centrifugal contribution) divided by density, ν is the kinematic viscosity, \mathbf{F} is an external force, $\boldsymbol{\Omega}$ is the possible rotation rate of the frame, and $-2\boldsymbol{\Omega} \times \mathbf{u}$ is therefore the Coriolis force.

The Navier-Stokes equations (7) are solved in a three-dimensional 2π -periodic cube C with a classical Fourier pseudo-spectral algorithm (see for instance [22, 23]). The code uses the 2/3-rule for dealiasing and third-order Adams-Bashforth scheme for time marching.

The periodic velocity field $\mathbf{u}(\mathbf{x})$ can be expanded as an infinite Fourier series

$$\mathbf{u}(\mathbf{x}) = \sum_{\mathbf{k}} \hat{\mathbf{u}}(\mathbf{k}) e^{i\mathbf{k} \cdot \mathbf{x}} \quad (8)$$

where \mathbf{k} represents now discrete wavevectors and $\hat{\mathbf{u}}(\mathbf{k}) = (2\pi)^{-3} \int_C \mathbf{u}(\mathbf{x}) e^{-i\mathbf{k} \cdot \mathbf{x}} d\mathbf{x}$ are the Fourier coefficients of $\mathbf{u}(\mathbf{x})$. $\hat{\mathbf{u}}(\mathbf{k})$ can be projected onto the Craya-Herring frame,

$$\hat{\mathbf{u}}(\mathbf{k}) = u^{(1)}(\mathbf{k}) \mathbf{e}^{(1)}(\mathbf{k}) + u^{(2)}(\mathbf{k}) \mathbf{e}^{(2)}(\mathbf{k}) \quad (9)$$

with no component of $\hat{\mathbf{u}}$ along $\mathbf{e}^{(3)}$ because of the incompressibility condition $\mathbf{k} \cdot \hat{\mathbf{u}}(\mathbf{k}) = 0$. $R_{ij}(\mathbf{r})$ is periodic too, and the tensor $E_{ij}(\mathbf{k}) = \langle \hat{u}_i^*(\mathbf{k}) \hat{u}_j(\mathbf{k}) \rangle$ represents its Fourier coefficients. The decomposition developed in section 2.1 for \hat{R}_{ij} may be repeated for E_{ij} with no formal difference. In addition, the spectral densities appearing in Eq. (4) are now linked to $\hat{\mathbf{u}}(\mathbf{k})$, *i.e.* $e(\mathbf{k}) = \langle \hat{\mathbf{u}}^*(\mathbf{k}) \cdot \hat{\mathbf{u}}(\mathbf{k}) \rangle / 2$, $h(\mathbf{k}) = \langle \hat{\boldsymbol{\omega}}(\mathbf{k}) \cdot \hat{\mathbf{u}}^*(\mathbf{k}) \rangle$, $z(\mathbf{k}) = \langle u^{(2)*}(\mathbf{k}) u^{(2)}(\mathbf{k}) - u^{(1)*}(\mathbf{k}) u^{(1)}(\mathbf{k}) \rangle / 2 + i \langle u_R^{(1)}(\mathbf{k}) u_R^{(2)}(\mathbf{k}) + u_I^{(1)}(\mathbf{k}) u_I^{(2)}(\mathbf{k}) \rangle$, where the subscripts R and I stand for real and imaginary parts. We compute the spherically integrated spectra as sums of the corresponding spectral densities in unitary-thickness shells. From the definition of vorticity and the Schwarz inequality one can show that a realizability condition holds : $|h(\mathbf{k})| \leq 2 |\mathbf{k}| e(\mathbf{k})$. Therefore, we define *relative helicity* as $H_{\text{rel}} = \langle H \rangle L_h / K$ where $K = \sum e(\mathbf{k})$ is the turbulent kinetic energy and L_h is a modified length scale (different from the integral length scale), defined from the spherically integrated kinetic energy spectrum as

$$L_h = \frac{1}{2} \frac{\sum E(k_i)}{\sum k_i E(k_i)} \quad (10)$$

so that, from the above inequality, $H_{\text{rel}} \leq 1$.

When performing direct numerical simulations, one would like to force turbulence for two reasons. First, this permits to reach higher Reynolds numbers than in freely decaying turbulence. Second, under some assumptions, statistics can then be obtained with time-averaging rather than ensemble averaging (see *e.g.* [24]) which would be very costly considering the fact that our refined statistics require a large number of samples. We forced our runs with the Euler forcing scheme [25, 26], which can be thought of as introducing three-dimensional large-scale vortices that evolve in time by interacting with each other—but not with the other scales of the flow—in a manner closer to actual inviscid turbulent nonlinear dynamics. The corresponding external force is unsteady and chaotic, the number of excited modes and the amount of injected helicity can be controlled.

The Euler scheme is inspired by truncated Euler dynamics [27] : the lowest-wavenumbers modes, corresponding to wavevectors \mathbf{k} such that $0 \leq |\mathbf{k}| \leq k_F$ (k_F is the largest forcing wavenumber), obey the three-dimensional incompressible Euler equations (eventually with background rotation) and are inde-

pendent of the other modes. Of course the modes corresponding to wavenumbers \mathbf{k} such that $|\mathbf{k}| > k_F$ are solutions of the incompressible Navier-Stokes equations and also depend on the modes in the Euler forcing sphere. Since energy and helicity are conserved within every nonlinear triadic interaction [28], in this truncated system total energy and helicity are conserved too. Background rotation does not affect this conservation property, since the Coriolis force has vanishing contributions in both energy and helicity evolution equations (for the truncated system as well as for every non-linear triadic interaction). For details about the Euler forcing and its implementation see [26].

4 Anisotropy induced by rotation

In this section we study the anisotropy that arises because of background rotation through 1024^3 resolution Euler-forced runs, see Table 1. Both the rotation rate vector $\mathbf{\Omega}$ and the fixed direction \mathbf{n} defining the Craya frame are in the z direction. In all runs presented in this table the spherically truncated Euler equation includes the Coriolis force, however we also performed runs without rotation in the Euler system and observed no significant change in the small scale anisotropy. Run S_{nh}^1 also has smaller Zeman wavenumber, and thus permits to study the anisotropic features of scales much smaller than the Zeman scale.

Figure 2 shows the kinetic energy directional-spectra, $E_i(k)$. We can observe a wide inertial range, with a slope close to $-5/3$ for runs S_{nh}^1 and S_h due to weak rotation. From this energetic point of view, large scales wavevectors closer to the horizontal plane $\mathbf{k} \cdot \mathbf{\Omega} = 0$ (red curve) hold more energy than wavevectors closer to $\mathbf{\Omega}$ (blue curve), indicating a trend towards two-dimensionalisation, as expected in rotating turbulence. However, in the large Rossby number case (run S_{nh}^1), small scales seem to recover isotropy since all directional spectra collapse on the spherically integrated spectrum.

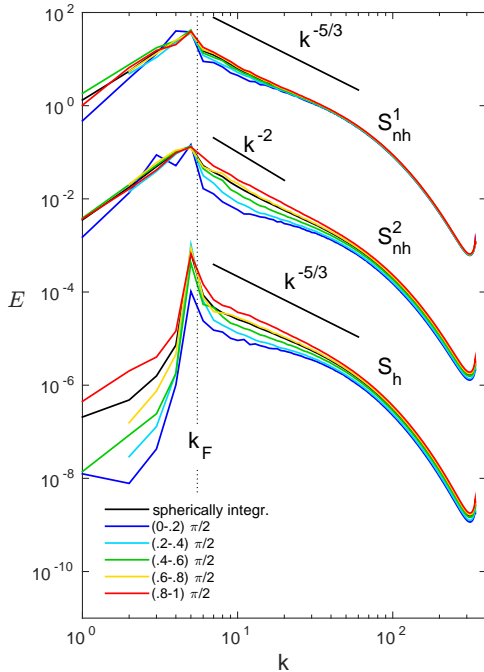


FIGURE 2 – Directional energy spectra $E_i(k)$ for the three runs considered.

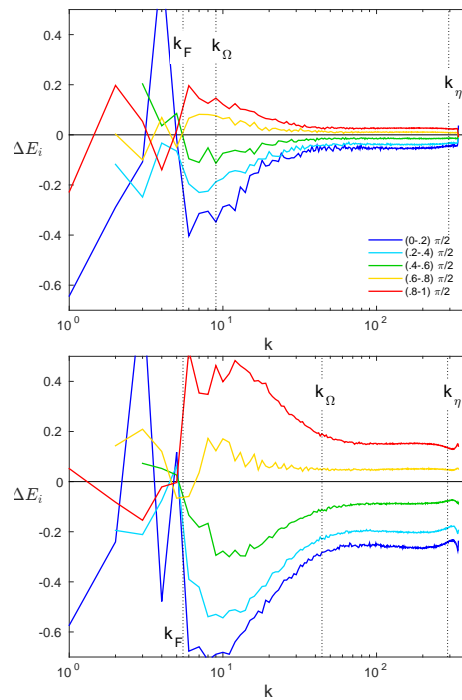


FIGURE 3 – Energy directional anisotropy $\Delta E_i(k)$ for : (a) run S_{nh}^1 ; (b) run S_{nh}^2 .

Run	Forcing	k_F	$k_{\max}\eta$	k_η	k_Ω	Re^λ	Re^L	Ro^ω	Ro^L	\mathcal{H}_{rel}	Resolution
S_{nh}^1	non-hel.	5.5	1.16	295	9.01	151	808	5.91	0.605	-2.85E-3	1024^3
S_{nh}^2	non-hel.	5.5	1.17	290	44.1	187	959	2.03	0.216	-5.27E-3	1024^3
S_{h}	helical	5.5	1.29	264	47.5	193	797	1.81	0.240	0.386	1024^3

TABLE 1 – Parameters used in the rotating turbulence simulations. k_{\max} is the maximal resolved wavenumber (after dealiasing), η is the Kolmogorov length scale corresponding to wavenumber $k_\eta = 1/\eta$. $k_\Omega = \left((2\Omega)^3/\epsilon\right)^{1/2}$ is the Zeman wavenumber. Re^λ and Re^L are the Reynolds numbers based on the Taylor-lengthscale and on the longitudinal integral lengthscale L , respectively. Ro^ω and Ro^L are the Rossby numbers defined in the Introduction. \mathcal{H}_{rel} refers to global relative helicity, *i.e.* it includes both the modes in the truncated system and the modes corresponding to wavenumbers outside the Euler sphere. The subscripts $_{\text{nh}}$ and $_{\text{h}}$ stand for non-helical and helical cases, respectively.

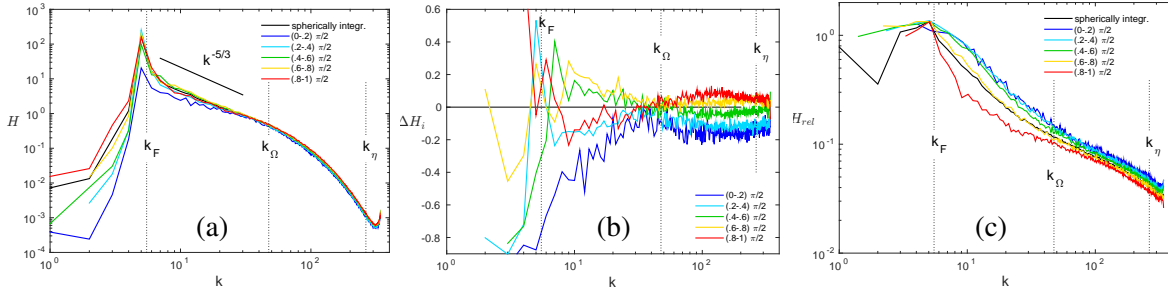


FIGURE 4 – Run S_{h} : (a) directional helicity spectra $H_i(k)$; (b) helicity directional anisotropy $\Delta H_i(k)$; (c) relative-helicity directional anisotropy $H_{\text{reli}}(k)$.

A more refined information can be obtained by measuring only the relative anisotropy in the energy spectrum : for this, we compute the scale-normalized departure between each directional spectrum and the corresponding average spectrum, $\Delta E_i(k) = (E_i(k) - E(k))/E(k)$. In Fig. 3 we present the relative directional energy anisotropy thus obtained for runs S_{nh}^1 and S_{nh}^2 (there is no substantial difference in energy directional anisotropy between run S_{h} and run S_{nh}^1). Surprisingly, it shows that even in the largest Rossby number case (run S_{nh}^1), the amplitude of the relative energy departure is still significant at small scales. A second important observation is that there seems to be two subranges in the inertial spectral range over which anisotropy behaves differently. In the first subrange, the maximal relative anisotropy in every sector decreases. Then, for wavenumbers greater than an intermediate value, the maximal relative anisotropy remains roughly constant. The separating wavenumber is clearly larger than k_Ω for run S_{nh}^1 (large Rossby number) and is close to k_Ω for the other runs, S_{nh}^2 and S_{h} , which have moderate Rossby numbers. Therefore, it is not clear how the separating scale between these two anisotropic ranges depends on the Zeman wavenumber.

Finally, we present helicity directional spectra $H_i(k)$, helicity directional anisotropy $\Delta H_i(k) = (H_i(k) - H(k))/H(k)$ and relative-helicity directional anisotropy $H_{\text{reli}}(k) = H_i(k)/(2kE_i(k))$ in Fig. 4. Figure 4(b) shows that at large scales the intermediate sectors hold more helicity than the horizontal and the vertical ones, while at small scales helicity is more concentrated in the sectors closer to the horizontal plane, a behaviour similar to energy directional anisotropy, see Fig. 3. Figure 4(b) also shows that helicity directional isotropy is recovered at some intermediate wavenumber. However, from

the viewpoint of relative helicity, Fig. 4(c), no directional isotropy is recovered, and—no matter the scale—sectors closer to the horizontal plane hold lower relative helicity.

5 Threshold wavenumber between two anisotropic ranges

In section 4, our analysis—that uses normalised indicators and includes simulations with different Rossby numbers—shows no isotropy recovery, in contrast with the classical dimensional argument and previous numerical results [8, 9] but in agreement with experiments [10]. Nevertheless, even if isotropy is not recovered at small scales in our simulations, two different anisotropic ranges with qualitatively different anisotropic features can be identified, see *e.g.* Figs. 2 and 3. The low-wavenumber range shows large-anisotropy decreasing with wavenumber, while the anisotropy level at larger wavenumbers is significantly lower, although not zero. Then, one may wonder if the threshold wavenumber between these two ranges has a specific physical interpretation. In order to answer this question, we analyse here a larger number of Euler-forced runs (17 runs with 512^3 resolution and 6 runs with 1024^3 resolution), with Ro^ω ranging from 0.67 to 9.6, Re^λ ranging from 73.9 to 416, and r_Ω/η ranging from 1.25 to 68. Note that this set also includes runs with different forcing scales ($k_F = 1.5, 3.5$ and 5.5), different relative helicity (ranging from 0 to 0.84), and runs that include or do not include the Coriolis force in the spherically truncated system.

First, we define a systematic method to compute the threshold wavenumber k_T , separating small-wavenumber (large anisotropy) and large-wavenumber (low anisotropy) ranges. Then, we investigate its dependence on the other parameters of the flow and look for a physical interpretation for k_T .

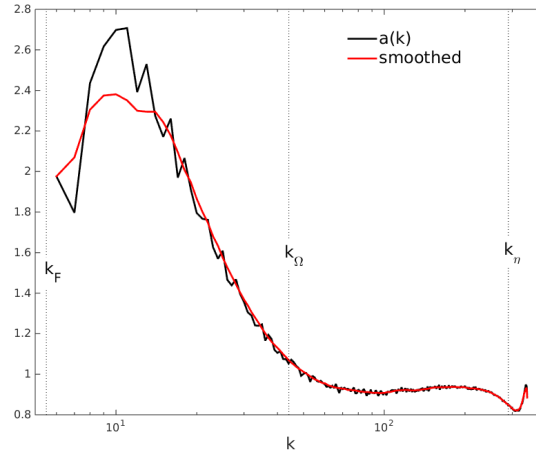
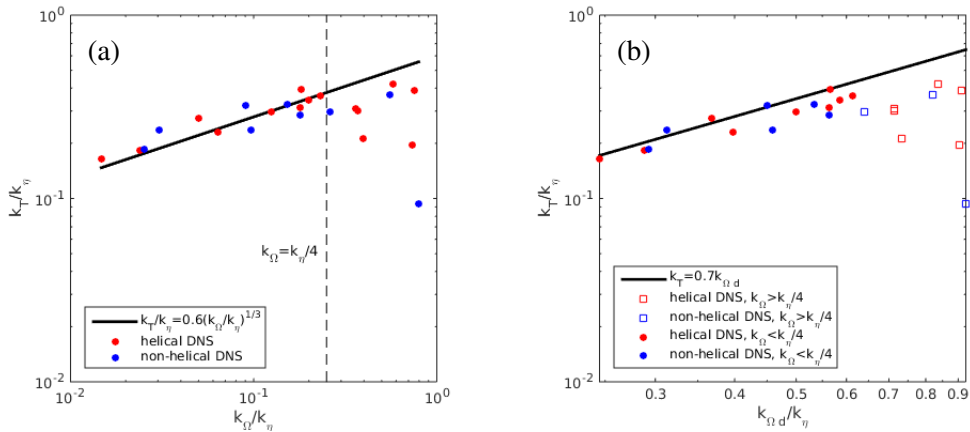
Since for every run five energy directional-anisotropy indicators $\Delta E_i(k)$ are available, we first reduce them to a single indicator $a(k)$. In particular, we normalise every $\Delta E_i(k)$ by its mean value over the range $k > k_F$, and then average them :

$$a(k) = \frac{1}{5} \sum_{i=1}^5 \frac{\Delta E_i(k)}{\langle \Delta E_i \rangle}. \quad (11)$$

Figure 5 shows the anisotropy indicator $a(k)$ corresponding to run S_{nh}^2 (Fig. 3(b)). In all rotating runs we found that $a(k)$ quickly decreases with wavenumber at large scales, then slowly increases with wavenumber, before reaching a plateau, at small scales. Therefore, we compute k_T as the wavenumber corresponding to the minimum of $a(k)$, after possible smoothing.

As a first attempt, it is natural to investigate the dependence of k_T on the Zeman wavenumber k_Ω , with the purpose of checking the existence of a range in which $k_T \sim k_\Omega$. In Fig. 6(a), k_T/k_η is plotted as a function of k_Ω/k_η . For $k_\Omega/k_\eta \lesssim 1/4$ (weak or moderate rotation), k_T/k_η clearly increases with k_Ω/k_η , with a power law of exponent $1/3$. For larger values of k_Ω/k_η , markers are rather scattered, and no clear trend is observed. One possible explanation for the existence of these two regimes is that, if rotation is too strong (or equivalently k_Ω/k_η is too large), the threshold wavenumber k_T is located in the dissipative range, whereas in the opposite case it is in the inertial range. These two ranges are phenomenologically different, and different laws can be expected in the two cases. The rest of our discussion will be performed in the regime $k_\Omega/k_\eta \lesssim 1/4$, in which $k_T/k_\eta \sim (k_\Omega/k_\eta)^{1/3}$. This amounts to discard the lowest Rossby number runs.

In brief, Fig. 6(a) shows two important results : first, depending on the closeness of k_Ω to k_η two sub-ranges with different behaviours are observed and second, in the low k_Ω range, k_T scales as $k_\Omega^{1/3} k_\eta^{2/3}$.

FIGURE 5 – Anisotropy indicator (defined by Eq. (11)) for run S_{nh}^2 .FIGURE 6 – k_T/k_η plotted as a function of (a) k_Ω/k_η , (b) $k_{\Omega d}/k_\eta$.

In this regime, k_T is therefore not proportional to k_Ω , and depends on the dissipative scale as well. Recalling from the Introduction that, from the definitions of $k_{\Omega d}$, k_Ω and k_η , $k_{\Omega d} = k_\Omega^{1/3} k_\eta^{2/3}$, this means that k_T scales as $k_{\Omega d}$. This result is confirmed by Fig. 6(b), which also shows that the factor between k_T and $k_{\Omega d}$ is close to 1, therefore :

$$k_T \approx k_{\Omega d} = \left(\frac{2\Omega}{\nu} \right)^{1/2}. \quad (12)$$

This relation definitely identifies k_T as the wavenumber at which the rotation time equals the characteristic dissipation time, provided that k_Ω/k_η is not too large (in practice, $k_\Omega \lesssim k_\eta/4$). In other words, at small wavenumbers anisotropy quickly decreases with the wavenumber, then reaches a minimum at $k = k_{\Omega d}$, after which it slowly increases before reaching a plateau up to the smallest resolved scales. Also recalling from the Introduction that, under the hypothesis $\omega' \sim \nu k_\eta^2$, Ro^ω should scale as $(k_\eta/k_\Omega)^{2/3}$, the above result, Eq. (12) yields : $k_T \sim k_\Omega Ro^\omega$. To check this, k_T/k_Ω is plotted against Ro^ω in Fig. 7(a). Again, this scaling is satisfied for the data corresponding to $k_\Omega < k_\eta/4$.

In order to make sure that the scaling law found above is not artificially induced by the forcing, further investigation is required. In fact, if rotation is too weak, the threshold wavenumber k_T may be close enough to k_F for the forcing scheme to affect its value. In Fig. 7(b), k_T/k_F is plotted as a function of k_Ω/k_F (runs for which $k_\Omega > k_\eta/4$ are not included). No trend is visible from these data, so that no forcing effect is detected. Such an effect might, however, be evidenced in simulations with larger forcing

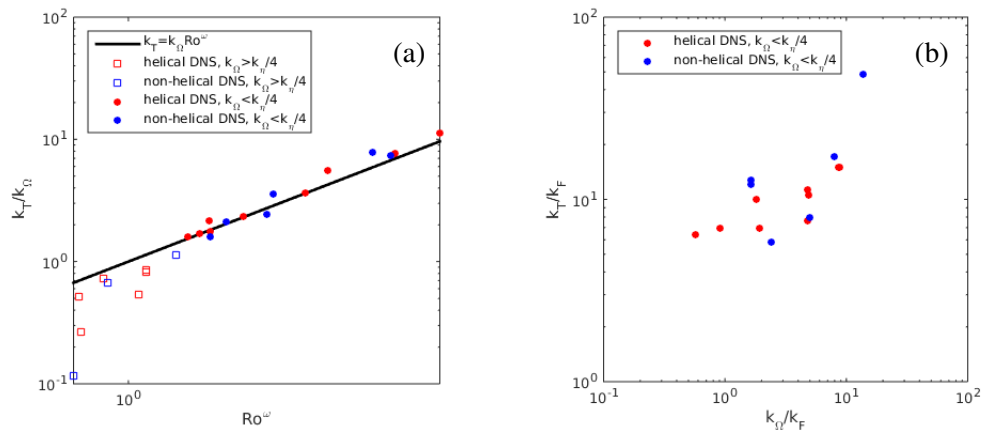


FIGURE 7 – (a) k_T/k_Ω plotted as a function of Ro^ω , (b) k_T/k_F plotted as a function of k_Ω/k_F .

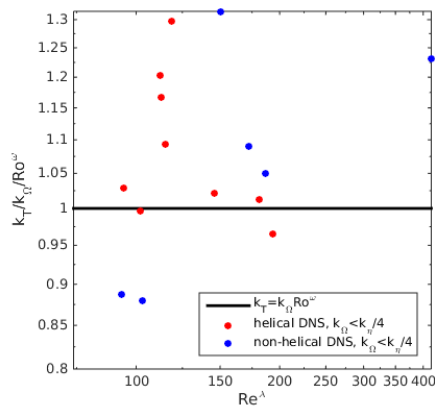


FIGURE 8 – Dependence of k_T scaling law on Reynolds number.

wavenumber or larger Rossby number.

Finally, we investigate the dependence of the k_T scaling law on the Reynolds number, see Fig. 8 in which $k_T/(k_\Omega Ro^\omega)$ is plotted as a function of Re^λ . As already shown in Fig. 7(a), this quantity is always close to one. Moreover, there is no correlation between it and Re^λ . It seems therefore that, in the range covered by our runs, the scaling law of k_T (Eq. (12)) does not depend on Reynolds number.

Note that in the asymptotic limit of infinite Reynolds number, according to our scaling law, $k_T \sim k_\Omega d \rightarrow \infty$ and thus only the low-wavenumber anisotropic range ($k < k_T$) should persist. In this range anisotropy decreases with wavenumber, which is possibly consistent with the classical argument according to which isotropy should be recovered at scales infinitely smaller than the Zeman scale (if the minimum of $a(k)$ tends to zero).

6 Summary and conclusions

In this work, we have investigated rotating turbulence in which anisotropy is produced by the action of the Coriolis force on the flow dynamics.

Since the anisotropy induced by rotation may concern all the scales in the flow, we have not quantified it by one-point statistics, but have instead considered multiscale statistics. More specifically, we have considered energy and helicity spectral densities, and have separated each of these two spectra into

directional contributions. The resulting directional energy spectra relate for instance to trends towards bidimensionalization or vertically-sheared horizontal flow. Helicity spectra further indicate the helical contents at the considered scale (or wavenumber).

We showed that in rotating turbulence, energy and helicity directional anisotropies are present at the smallest scales of the flow even at large Rossby numbers (even though the anisotropy level decreases as the Rossby number increases). However, we identified two different wavenumber ranges in which anisotropy evolves differently : it decreases at increasing wavenumber at larger scales, then becomes minimal before slowly increasing with wavenumber, and finally reaches a plateau at the smallest scales. Finally, we identified the characteristic scale separating these two ranges. When it is large enough, we have identified it as the scale at which dissipative effects are of the same order as those of rotation. This provides not only a qualitative but also an accurate quantitative threshold separating the two anisotropic subranges. This behaviour is observed consistently at all the Reynolds numbers we have examined.

In the asymptotic limit of infinite Reynolds number our results predict anisotropy to monotonously decrease at increasing wavenumber, a scenario possibly consistent with the classical dimensional argument about isotropy recovery at scales much smaller than the Zeman scale.

Acknowledgements

The data used in this work were computed thanks to computational time provided by GENCI/CINES under project number A0012A2206 and by the FLMSN HPC mesocenter in Lyon, France, funded by the equip@Meso project.

Références

- [1] N. Mordant, J.-F. Pinton and F. Chillà. Characterization of Turbulence in a Closed Flow. *J. Phys. II France*, 7(11) : 1729–1742, 1997.
- [2] F.S. Godeferd and F. Moisy. Structure and Dynamics of Rotating Turbulence : A Review of Recent Experimental and Numerical Results. *ASME. Appl. Mech. Rev.*, 67(3) : 030802–030802, 2015.
- [3] O. Zeman. A note on the spectra and decay of rotating homogeneous turbulence. *Phys. Fluids*, 6 : 3221, 1994.
- [4] J. D. Woods. Diffusion due to fronts in the rotation sub-range of turbulence in the seasonal thermocline. *La Houille Blanche*, 29 : 589–597, 1974.
- [5] Vassilicos, JC. Dissipation in Turbulent Flows. *ANNUAL REVIEWS*, 95–114, 2015.
- [6] Bos, Wouter JT, Shao, Liang and Bertoglio, J-P. Spectral imbalance and the normalized dissipation rate of turbulence. *Physics of Fluids*, 19(4) : 045101, 2007.
- [7] Susumu Goto and J.C. Vassilicos. Energy dissipation and flux laws for unsteady turbulence. *Physics Letters A*, 379(16–17) : 1144–1148, 2015.
- [8] Alexandre Delache, Claude Cambon and Fabien Godeferd. Scale by scale anisotropy in freely decaying rotating turbulence. *Physics of Fluids*, 26(2) : 025104, 2014.
- [9] P. D. Mininni, D. Rosenberg and A. Pouquet. Isotropization at small scales of rotating helically driven turbulence. Cambridge University Press, 699 : 263–279, 2012.

- [10] Lamriben, Cyril, Cortet, Pierre-Philippe and Moisy, Frédéric. Direct Measurements of Anisotropic Energy Transfers in a Rotating Turbulence Experiment. *Phys. Rev. Lett.*, 107 : 024503, 2011.
- [11] Lumley, John L. and Newman, Gary R.. The return to isotropy of homogeneous turbulence. *Journal of Fluid Mechanics*, 82(1) : 161–178, 1977.
- [12] A. Craya. Contribution à l'analyse de la turbulence associée à des vitesses moyennes. *P. S. T.*, 345, 1958.
- [13] Sagaut, Pierre and Cambon, Claude. *Homogeneous Turbulence Dynamics*. Cambridge University Press, 2008.
- [14] C. Cambon, N. N. Mansour and F. S. Godeferd. Energy transfer in rotating turbulence. *J. Fluid Mech.*, 337 : 303, 1997.
- [15] Fabian Waleffe. Inertial transfers in the helical decomposition. *Physics of Fluids A : Fluid Dynamics*, 5(3) : 677–685, 1993.
- [16] Favier, B., Godeferd, F. S. and Cambon, C. and Delache, A. and Bos, W. J. T.. Quasi-static magnetohydrodynamic turbulence at high Reynolds number. *Journal of Fluid Mechanics*, 681 : 434–461, 2011.
- [17] H. K. Moffatt. The degree of knottedness of tangled vortex lines. *Journal of Fluid Mechanics*, 35(1) : 117–129, 1969.
- [18] H K Moffatt and A Tsinober. Helicity in Laminar and Turbulent Flow. *Annual Review of Fluid Mechanics*, 24(1) : 281–312, 1992.
- [19] Galtier, Sébastien. Theory for helical turbulence under fast rotation. *Phys. Rev. E*, 89 : 041001, 2014.
- [20] Cambon, C. and Jacquin, L.. Spectral approach to non-isotropic turbulence subjected to rotation. *Journal of Fluid Mechanics*, 202 : 295–317, 1989.
- [21] Godeferd, F. S. and Staquet, C.. Statistical modelling and direct numerical simulations of decaying stably stratified turbulence. Part 2. Large-scale and small-scale anisotropy. *Journal of Fluid Mechanics*, 486 : 115–159, 2003.
- [22] Orszag, Steven A. and Patterson, G. S.. Numerical Simulation of Three-Dimensional Homogeneous Isotropic Turbulence. *Phys. Rev. Lett.*, 28 : 76–79, 1972.
- [23] A. Vincent and M. Meneguzzi. The spatial structure and statistical properties of homogeneous turbulence. *J. Fluid Mech.*, 225 : 1–20, 1991.
- [24] J. Mathieu and J. Scott. *An Introduction to Turbulent Flow*. Cambridge University Press, 2000.
- [25] Alain Pumir. A numerical study of pressure fluctuations in three-dimensional, incompressible, homogeneous, isotropic turbulence. *Physics of Fluids*, 6(6) : 2071–2083, 1994.
- [26] D. Vallefucio, A. Naso and F.S. Godeferd. Small-scale anisotropy induced by spectral forcing and by rotation in non-helical and helical turbulence. (in preparation).
- [27] Cichowlas, Cyril, Bonaiti, Pauline and Debbasch, Fabrice and Brachet, Marc. Effective Dissipation and Turbulence in Spectrally Truncated Euler Flows. *Phys. Rev. Lett.*, 95 : 264502, 2005.
- [28] Kraichnan, Robert H.. Helical turbulence and absolute equilibrium. *Journal of Fluid Mechanics*, 59(4) : 745–752, 1973.
1995, pp. 3–6.